AAS 15-027

EXPERIMENTAL VALIDATION OF AN INERTIA-FREE CONTROLLER AND A MULTIPLICATIVE EKF FOR POSE TRACKING AND ESTIMATION BASED ON DUAL QUATERNIONS

Alfredo Valverde,[*] Nuno Filipe,[†] Michail Kontitsis,[‡] and Panagiotis Tsiotras[§]

This paper presents the experimental results from the validation of a dual quaternion inertia-free adaptive controller, in combination with a continuous/discrete Dual Quaternion-Multiplicative Extended Kalman Filter (DQ-MEKF) for spacecraft pose estimation and tracking. The experiments were conducted on the Autonomous Spacecraft Testing of Robotic Operations in Space (ASTROS) facility, an experimental 5-DOF platform located at the Georgia Institute of Technology, equipped with rate gyros, inertial measurement unit, reaction wheels, cameras, and cold-gas thrusters. Experimental results are given for a maneuver in closed-loop, and are evaluated using a VICON optical tracking system.

INTRODUCTION

The demand for reliable systems in the spacecraft industry benefits from innovative and efficient ways of testing and validating the use of guidance, navigation and control algorithms under 1g conditions. Air-bearing systems, a common method for experimental validation of spacecraft attitude control, date back to the beginning of the space race.[1] In the past, various 3-DOF experimental testbeds have allowed the implementation and study of various attitude control algorithms.[2,3,4] Other 3-DOF testbeds allow for two linear and one rotational degrees of freedom, tackling problems like autonomous rendezvous and docking or formation flight.[1,5]

Attempts at implementing a 6-DOF platform have been made, but these are not reported as operational under 1g conditions to this writing.[6,7,8] Five degrees of freedom (5-DOF) platforms still represent one of the most realistic methods for ground testing of satellite GNC algorithms. The platform used in this paper, the Autonomous Spacecraft Testing of Robotic Operations in Space (ASTROS), located at the Dynamics and Control Systems Laboratory (DCSL) at the Georgia Institute of Technology, consists of a platform with linear and spherical air-bearings that are able to simulate almost frictionless operations. The ASTROS platform is equipped with rate gyros, an inertial measurement unit and cold-gas thrusters. The facility uses a VICON system that provides real-time position and attitude information. In addition, a high fidelity simulation has been developed to study the performance of the ASTROS platform and the feasibility of maneuvers, drastically decreasing failed experimental attempts and providing a reliable method to quickly explore new algorithms.

The adaptive controller used in the platform in this paper uses a dual quaternion description to track a reference pose (i.e., attitude and position) under mass and inertia matrix uncertainty.[9]

[*] Ph.D. Student, School of Aerospace Engineering, Georgia Institute of Technology
[†] Ph.D. Candidate, School of Aerospace Engineering, Georgia Institute of Technology
[‡] Postdoctoral Research Associate, School of Aerospace Engineering, Georgia Institute of Technology
[§] Dean's Professor, School of Aerospace Engineering, Georgia Institute of Technology

The controller achieves almost global asymptotic stability of the tracking error. Dual quaternions extend their more well-known counterpart, namely, quaternions, and are able to simultaneously – and compactly– represent attitude and position. A dual quaternion is of the form $q_r + \epsilon q_d$, where the real and dual parts, q_r and q_d respectively, are quaternions and ϵ is a nilpotent operator, which has index of nilpotency of two (i.e., $\epsilon^2 = 0$). Dual quaternions have shown great applicability in the areas of inertial navigation, rigid body control, computer vision, and inverse kinematic analysis, amongst others.[9] A major advantage of the use of dual quaternions is the natural coupling of the linear and rotational dynamics, through an algebra that closely resembles that of quaternions. Based on this analogy, the formulation of new dual quaternion control laws is more approachable than, say, Lie algebraic methods that formulate the problem on SE(3),[10,11] additionally yielding compact and numerically stable expressions.

One of the advantages of the tracking controller tested is that it also provides sufficient conditions on the reference trajectory that guarantee mass and inertia matrix identification. An in-depth description and derivation of the controller, as well as simulation results, are given in Refs. [9, 10, 12]. The tracking controller is tested in operation with an estimator that is also based on dual quaternions. This Dual Quaternion-Multiplicative Extended Kalman Filter (DQ-MEKF) is described in Refs. [13, 10]. The DQ-MEKF uses an error unit dual quaternion, which leads to the use of a six-component state vector (instead of eight as in Refs. [14, 15, 16, 17]). The DQ-MEKF is a *continuous-discrete extended Kalman filter* (continuous state and covariance matrix propagation between discrete measurements), integrating measurements of different sensors at different update rates. It takes continuous-time angular velocity and linear acceleration measurements with noise and bias from the rate-gyros and the IMU, respectively, and discrete-time pose measurements with noise from the VICON system.

MATHEMATICAL PRELIMINARIES

The formulations presented in this paper are based on dual quaternion algebra. A dual quaternion $\boldsymbol{q} \in \mathbb{H}_d$ has the form $\boldsymbol{q} = q_r + \epsilon q_d$, where the real and dual parts, q_r and q_d are quaternions (i.e., $q_r,\, q_d \in \mathbb{H}$), q_r is a unit quaternion, and $\epsilon^2 = 0$. The basic operations on dual quaternions are presented here for completeness, though Ref. [10] may be used for further details.

$$\text{Addition: } \boldsymbol{a} + \boldsymbol{b} = (a_r + b_r) + \epsilon(a_d + b_d) \tag{1}$$

$$\text{Multiplication by a scalar: } \lambda\boldsymbol{a} = (\lambda a_r) + \epsilon(\lambda a_d) \tag{2}$$

$$\text{Multiplication: } \boldsymbol{ab} = (a_r b_r) + \epsilon(a_r b_d + a_d b_r) \tag{3}$$

$$\text{Conjugation: } \boldsymbol{a}^{*} = a_r^* + \epsilon a_d^* \tag{4}$$

$$\text{Swap: } \boldsymbol{a}^{\mathsf{s}} = a_d + \epsilon a_r \tag{5}$$

$$\text{Dot product: } \boldsymbol{a} \cdot \boldsymbol{b} = \frac{1}{2}(\boldsymbol{a}\boldsymbol{b}^{*} + \boldsymbol{b}\boldsymbol{a}^{*}) \tag{6}$$

$$\text{Cross product: } \boldsymbol{a} \times \boldsymbol{b} = \frac{1}{2}(\boldsymbol{a}\boldsymbol{b} - \boldsymbol{b}^{*}\boldsymbol{a}^{*}) \tag{7}$$

$$\text{Circle product: } \boldsymbol{a} \circ \boldsymbol{b} = a_r \cdot b_r + a_d \cdot b_d \tag{8}$$

$$\text{Scalar part: } \mathrm{sc}(\boldsymbol{a}) = \mathrm{sc}(a_r) + \mathrm{sc}(a_d) \tag{9}$$

$$\text{Vector part: } \mathrm{vec}(\boldsymbol{a}) = \mathrm{vec}(a_r) + \mathrm{vec}(a_d) \tag{10}$$

In addition to the above, the following two norms can be defined on $\mathbb{H}_d$ as follows: a) the dual norm, defined by $||\boldsymbol{a}||_d^2 = \boldsymbol{a}\boldsymbol{a}^*$ and b) the norm $||\boldsymbol{a}||^2 = \boldsymbol{a} \circ \boldsymbol{a}$.

The multiplication of a matrix $M \in \mathbb{R}^{8\times 8}$ with a dual quaternion is defined as $M \star \boldsymbol{q} = (M_{11} * q_r + M_{12} * q_d) + \epsilon(M_{21} * q_r + M_{22} * q_d)$, where

$$M = \begin{bmatrix} M_{11} & M_{12} \\ M_{21} & M_{22} \end{bmatrix}, \quad M_{11}, M_{12}, M_{21}, M_{22} \in \mathbb{R}^{4\times 4}, \tag{11}$$

and where the operation $*$ is defined as

$$N * q = (N_{11}q_0 + N_{12}\overline{q}, N_{21}q_0 + N_{22}\overline{q}), \quad N = \begin{bmatrix} N_{11} & N_{12} \\ N_{21} & N_{22} \end{bmatrix} \in \mathbb{R}^{4\times 4}, \tag{12}$$

and $N_{11} \in \mathbb{R}$, $N_{12} \in \mathbb{R}^{1\times 3}$, $N_{21} \in \mathbb{R}^{3\times 1}$, and $N_{21} \in \mathbb{R}^{3\times 3}$. The $\star$ operation is analogous to multiplication between an 8-by-8 matrix and a vector in $\mathbb{R}^8$. In addition, the notation $\overline{\cdot} : \mathbb{H}_d \to \mathbb{R}^6$ applied on a dual quaternion $\boldsymbol{a} = a_r + \epsilon a_d$, where $a_r = (a_{r,0}, \overline{a}_r)$ and $a_d = (a_{d,0}, \overline{a}_d)$, is defined as $\overline{\boldsymbol{a}} = [\overline{a}_r^\mathsf{T}, \overline{a}_d^\mathsf{T}]^\mathsf{T} \in \mathbb{R}^6$. See ale Ref. [10]. Furthermore, for the set of vector quaternions, $\mathbb{H}^v$, the notation $[\,\cdot\,]^\times : \mathbb{H}^v \to \mathbb{R}^{4\times 4}$ is defined as

$$[a]^\times = \begin{bmatrix} 0 & 0_{1\times 3} \\ 0_{3\times 1} & \overline{a}^\times \end{bmatrix}, \quad \text{where} \quad \overline{a}^\times = \begin{bmatrix} 0 & -a_3 & a_2 \\ a_3 & 0 & -a_1 \\ -a_2 & a_1 & 0 \end{bmatrix}. \tag{13}$$

Moreover, the notation $[\,\widetilde{\cdot}\,] : \mathbb{H} \to \mathbb{R}^{3\times 3}$ is defined as $[\widetilde{a}] = a_0 I_{3\times 3} + \overline{a}^\times$.

A dual quaternion can store attitude and position information. For example, given the frames I and B, the *unit* dual quaternion $\boldsymbol{q}_{\mathrm{B/I}}$ satisfies

$$\boldsymbol{q}_{\mathrm{B/I}} = q_{\mathrm{B/I},r} + \epsilon q_{\mathrm{B/I},d} = q_{\mathrm{B/I}} + \epsilon \frac{1}{2} r^{\mathrm{I}}_{\mathrm{B/I}} q_{\mathrm{B/I}} = q_{\mathrm{B/I}} + \epsilon \frac{1}{2} q_{\mathrm{B/I}} r^{\mathrm{B}}_{\mathrm{B/I}}, \tag{14}$$

where $q_{\mathrm{B/I}}$ is the unit quaternion representing the relative orientation of the B frame with respect to the I frame, and $r^{\mathrm{X}}_{\mathrm{Y/Z}}$ is the quaternion representing the vector from the origin of the Z-frame to the origin of the Y-frame expressed in the X-frame. Furthermore, the dual velocity compactly stores linear and angular velocity information by

$$\boldsymbol{\omega}^{\mathrm{X}}_{\mathrm{Y/Z}} = \omega^{\mathrm{X}}_{\mathrm{Y/Z}} + \epsilon \left(v^{\mathrm{X}}_{\mathrm{Y/Z}} + \omega^{\mathrm{X}}_{\mathrm{Y/Z}} \times r^{\mathrm{X}}_{\mathrm{X/Y}} \right), \tag{15}$$

where $v^{\mathrm{X}}_{\mathrm{Y/Z}}$ and $\omega^{\mathrm{X}}_{\mathrm{Y/Z}}$ are the linear and angular velocities of the Y-frame with respect to the Z-frame expressed in the X-frame respectively. The quaternion representation of a vector $\bar{v} \in \mathbb{R}^3$ is $v = (0, \bar{v}^\mathsf{T})^\mathsf{T}$, i.e., a quaternion with zero scalar part. With this definition of dual velocity, the relative translational and rotational kinematic equations between two frames, say, B and D are given by

$$\dot{\boldsymbol{q}}_{\mathrm{B/D}} = \tfrac{1}{2} \boldsymbol{q}_{\mathrm{B/D}} \boldsymbol{\omega}^{\mathrm{B}}_{\mathrm{B/D}} = \tfrac{1}{2} \boldsymbol{\omega}^{\mathrm{D}}_{\mathrm{B/D}} \boldsymbol{q}_{\mathrm{B/D}}, \tag{16}$$

which are analogous to the quaternion representation of the rotational(-only) kinematic equations.[10] Furthermore, the dual quaternion representation of the relative rotational and translational dynamic equations of motion of a rigid body is given by[10]

$$\begin{aligned} (\dot{\boldsymbol{\omega}}^{\mathrm{B}}_{\mathrm{B/D}})^{\mathsf{s}} = {} & (M^{\mathrm{B}})^{-1} \star (\boldsymbol{f}^{\mathrm{B}} - (\boldsymbol{\omega}^{\mathrm{B}}_{\mathrm{B/D}} + \boldsymbol{\omega}^{\mathrm{B}}_{\mathrm{D/I}}) \times (M^{\mathrm{B}} \star ((\boldsymbol{\omega}^{\mathrm{B}}_{\mathrm{B/D}})^{\mathsf{s}} + (\boldsymbol{\omega}^{\mathrm{B}}_{\mathrm{D/I}})^{\mathsf{s}})) \\ & - M^{\mathrm{B}} \star (\boldsymbol{q}^*_{\mathrm{B/D}} \dot{\boldsymbol{\omega}}^{\mathrm{D}}_{\mathrm{D/I}} \boldsymbol{q}_{\mathrm{B/D}})^{\mathsf{s}} - M^{\mathrm{B}} \star (\boldsymbol{\omega}^{\mathrm{B}}_{\mathrm{D/I}} \times \boldsymbol{\omega}^{\mathrm{B}}_{\mathrm{B/D}})^{\mathsf{s}}) \end{aligned} \tag{17}$$

where $\boldsymbol{f}^{\mathrm{B}} = f^{\mathrm{B}} + \epsilon\tau^{\mathrm{B}}$ is the total external dual force applied to the body about its center of mass expressed in the body frame, $\overline{f}^{\mathrm{B}} \in \mathbb{R}^3$ is the total external force vector applied to the body expressed in the body frame, $\overline{\tau}^{\mathrm{B}} \in \mathbb{R}^3$ the total external moment vector applied to the body about its center of mass expressed in the body frame, $M^{\mathrm{B}} = \mathrm{diag}\left(1, mI_{3\times 3}, 1, \bar{I}^{\mathrm{B}}\right)$ is the dual inertia matrix, m is the mass and $\bar{I}^{\mathrm{B}} \in \mathbb{R}^{3\times 3}$ is the inertia matrix of the body about its center of mass written in the body frame. It is worth noting that Equation (17) is the dual quaternion counterpart to

$$\dot{\omega}^{\mathrm{B}}_{\mathrm{B/D}} = (I^{\mathrm{B}})^{-1} * (\tau^{\mathrm{B}} - (\omega^{\mathrm{B}}_{\mathrm{B/D}} + \omega^{\mathrm{B}}_{\mathrm{D/I}}) \times (I^{\mathrm{B}} * (\omega^{\mathrm{B}}_{\mathrm{B/D}} + \omega^{\mathrm{B}}_{\mathrm{D/I}}))) - q^*_{\mathrm{B/D}}\dot{\omega}^{\mathrm{D}}_{\mathrm{D/I}}q_{\mathrm{B/D}} - \omega^{\mathrm{B}}_{\mathrm{D/I}} \times \omega^{\mathrm{B}}_{\mathrm{B/D}}. \tag{18}$$

MASS AND INERTIA FREE ADAPTIVE CONTROLLER

The adaptive pose-tracking controller used for the experiments has been documented in Ref. [9]. This controller uses a dual quaternion formulation to ensure (almost) globally asymptotic stability of the pose-tracking error without need for mass or inertia matrix information. The basics of this controller are provided below for completeness.

The feedback control law used in this experiment is given by

$$\begin{aligned}\boldsymbol{f}^{\mathrm{B}}_c = &- \mathrm{vec}(\boldsymbol{q}^*_{\mathrm{B/D}}(\boldsymbol{q}^{\mathsf{s}}_{\mathrm{B/D}} - \mathbf{1}^{\mathsf{s}})) - K_d \star \boldsymbol{s}^{\mathsf{s}} + \boldsymbol{\omega}^{\mathrm{B}}_{\mathrm{B/I}} \times (\widehat{M^{\mathrm{B}}} \star (\boldsymbol{\omega}^{\mathrm{B}}_{\mathrm{B/I}})^{\mathsf{s}}) \\ &+ \widehat{M^{\mathrm{B}}} \star (\boldsymbol{q}^*_{\mathrm{B/D}}\dot{\boldsymbol{\omega}}^{\mathrm{D}}_{\mathrm{D/I}}\boldsymbol{q}_{\mathrm{B/D}})^{\mathsf{s}} + \widehat{M^{\mathrm{B}}} \star (\boldsymbol{\omega}^{\mathrm{B}}_{\mathrm{D/I}} \times \boldsymbol{\omega}^{\mathrm{B}}_{\mathrm{B/D}})^{\mathsf{s}} - \widehat{M^{\mathrm{B}}} \star (K_p \star \frac{d}{dt}(\boldsymbol{q}^*_{\mathrm{B/D}}(\boldsymbol{q}^{\mathsf{s}}_{\mathrm{B/D}} - \mathbf{1}^{\mathsf{s}}))),\end{aligned} \tag{19}$$

where $s = \boldsymbol{\omega}^{\mathrm{B}}_{\mathrm{B/D}} + K_p \star (\boldsymbol{q}^*_{\mathrm{B/D}}(\boldsymbol{q}^{\mathsf{s}}_{\mathrm{B/D}} - \mathbf{1}^{\mathsf{s}}))^{\mathsf{s}}$,

$$K_p = \begin{bmatrix} K_r & 0_{4\times 4} \\ 0_{4\times 4} & K_q \end{bmatrix}, \quad K_d = \begin{bmatrix} K_v & 0_{4\times 4} \\ 0_{4\times 4} & K_\omega \end{bmatrix},$$

$$K_r = \begin{bmatrix} 0 & 0_{1\times 3} \\ 0_{3\times 1} & \bar{K}_r \end{bmatrix}, K_q = \begin{bmatrix} 0 & 0_{1\times 3} \\ 0_{3\times 1} & \bar{K}_q \end{bmatrix}, K_v = \begin{bmatrix} 0 & 0_{1\times 3} \\ 0_{3\times 1} & \bar{K}_v \end{bmatrix}, K_\omega = \begin{bmatrix} 0 & 0_{1\times 3} \\ 0_{3\times 1} & \bar{K}_\omega \end{bmatrix},$$

$\bar{K}_r, \bar{K}_q, \bar{K}_v, \bar{K}_\omega \in \mathbb{R}^{3\times 3}$ are symmetric positive-definite matrices, and $\widehat{M^{\mathrm{B}}}$ is an estimate of the dual inertia matrix updated according to:

$$\begin{aligned}\frac{d}{dt}v(\widehat{M^{\mathrm{B}}}) = K_i \Bigg[&- h((\boldsymbol{s} \times \boldsymbol{\omega}^{\mathrm{B}}_{\mathrm{B/I}}), (\boldsymbol{\omega}^{\mathrm{B}}_{\mathrm{B/I}})^{\mathsf{s}}) \\ &+ h\left(\boldsymbol{s}^{\mathsf{s}}, -(\boldsymbol{q}^*_{\mathrm{B/D}}\dot{\boldsymbol{\omega}}^{\mathrm{D}}_{\mathrm{D/I}}\boldsymbol{q}_{\mathrm{B/D}})^{\mathsf{s}} - (\boldsymbol{\omega}^{\mathrm{B}}_{\mathrm{D/I}} \times \boldsymbol{\omega}^{\mathrm{B}}_{\mathrm{B/D}})^{\mathsf{s}} + K_p \star \frac{d(\boldsymbol{q}^*_{\mathrm{B/D}}(\boldsymbol{q}^{\mathsf{s}}_{\mathrm{B/D}} - \mathbf{1}^{\mathsf{s}}))}{dt}\right)\Bigg].\end{aligned} \tag{20}$$

The function $v(M^{\mathrm{B}})$ is a linearized version of the dual inertia matrix defined by $v(M^{\mathrm{B}}) = [I_{11}, I_{12}, I_{13}, I_{22}, I_{23}, I_{33}, m]^{\mathsf{T}}$, the function $h(\boldsymbol{a}, \boldsymbol{b})$ is defined as $h(\boldsymbol{a}, \boldsymbol{b})^{\mathsf{T}}v(M^{\mathrm{B}}) = \boldsymbol{a} \circ (M^{\mathrm{B}} \star \boldsymbol{b})$ and K_i is a 7-by-7 positive-definite matrix gain. For the proof of this result, see Ref. [9].

DUAL QUATERNION-MULTIPLICATIVE EXTENDED KALMAN FILTER

The DQ-MEKF used in this experiment is a continuous-discrete EKF that takes continuous-time angular velocity and linear acceleration measurements with noise and bias from the rate-gyros and the IMU, respectively, and discrete-time pose measurements with noise from the VICON system.[13] A summary of the equations of the DQ-MEKF is provided here, but the reader is referred to Ref. [13] for a complete description of the DQ-MEKF. The state and process noise vectors are

$$x = \begin{bmatrix} \overline{\delta\boldsymbol{q}_{\mathrm{B/I}}}^{\mathsf{T}} & \overline{\boldsymbol{b}}_{\boldsymbol{\omega}}^{\mathsf{T}} & \overline{b}_n^{\mathsf{T}} \end{bmatrix}^{\mathsf{T}} \in \mathbb{R}^{15} \quad \text{and} \quad w = \begin{bmatrix} \overline{\boldsymbol{\eta}}_{\boldsymbol{\omega}}^{\mathsf{T}} & \overline{\eta}_{b_\omega}^{\mathsf{T}} & \overline{\eta}_n^{\mathsf{T}} & \overline{\eta}_{b_n}^{\mathsf{T}} \end{bmatrix}^{\mathsf{T}} \in \mathbb{R}^{15}, \tag{21}$$

where $\delta \boldsymbol{q}_{\mathrm{B/I}} = \hat{\boldsymbol{q}}^*_{\mathrm{B/I}} \boldsymbol{q}_{\mathrm{B/I}}$ is the dual error quaternion between the current best guess $\hat{\boldsymbol{q}}_{\mathrm{B/I}}$ and the true dual quaternion $\boldsymbol{q}_{\mathrm{B/I}}$, $\boldsymbol{b_\omega} = b_\omega + \epsilon b_v$ is the dual bias, $b_\omega = (0, \bar{b}_\omega)$, $\bar{b}_\omega \in \mathbb{R}^3$ is the bias of the angular velocity measurement, $b_v = (0, \bar{b}_v)$, $\bar{b}_v \in \mathbb{R}^3$ is the bias of the linear velocity measurement, $b_n = (0, \bar{b}_n)$, and $\bar{b}_n \in \mathbb{R}^3$ is the bias of the specific force measurement. Also, $\boldsymbol{\eta_\omega} = \eta_\omega + \epsilon \eta_v$, $\eta_\omega = (0, \overline{\eta}_\omega)$, $\overline{\eta}_\omega \in \mathbb{R}^3$ is the noise of the angular velocity measurements assumed to be a zero-mean Gaussian white noise process, $\eta_v = (0, \overline{\eta}_v)$, $\overline{\eta}_v \in \mathbb{R}^3$ is the noise of the linear velocity measurements assumed to be a zero-mean Gaussian white noise process, $\overline{\eta}_n \in \mathbb{R}^3$ is the noise of the specific force measurement assumed to be a Gaussian white noise process, and $\overline{\eta}_{b_\omega} \in \mathbb{R}^3$ and $\overline{\eta}_{b_n} \in \mathbb{R}^3$ are also zero-mean Gaussian white noise processes that drive the corresponding biases by $\dot{\bar{b}}_\omega = \overline{\eta}_{b_\omega}$ and $\dot{\bar{b}}_n = \overline{\eta}_{b_n}$ respectively.

The state equations of the DQ-MEKF are modeled as $\dot{x}(t) = f(x(t), t) + g(x(t), t)w$, where

$$
f(x(t),t) = \begin{bmatrix} \overline{-\frac{1}{2}\hat{\boldsymbol{\omega}}^{\mathrm{B}}_{\mathrm{B/I}} \delta \boldsymbol{q}_{\mathrm{B/I}} + \frac{1}{2}\delta \boldsymbol{q}_{\mathrm{B/I}} \hat{\boldsymbol{\omega}}^{\mathrm{B}}_{\mathrm{B/I}} + \frac{1}{2}\delta \boldsymbol{q}_{\mathrm{B/I}} \hat{\boldsymbol{b}}_{\boldsymbol{\omega}} - \frac{1}{2}\delta \boldsymbol{q}_{\mathrm{B/I}} \boldsymbol{b}_{\boldsymbol{\omega}}} \\ 0_{3\times1} \\ \overline{-(\hat{\omega}^{\mathrm{B}}_{\mathrm{B/I}} + \hat{b}_\omega - b_\omega)\times b_v - c(\hat{n}^{\mathrm{B}}_{\mathrm{A/I}} + \hat{b}_n - b_n) + \delta q^*_{\mathrm{B/I}} \hat{q}^*_{\mathrm{B/I}} g^{\mathrm{I}} \hat{q}_{\mathrm{B/I}} \delta q_{\mathrm{B/I}} + (\hat{\omega}^{\mathrm{B}}_{\mathrm{B/I}} + \hat{b}_\omega - b_\omega)\times((\hat{\omega}^{\mathrm{B}}_{\mathrm{B/I}} + \hat{b}_\omega - b_\omega)\times r^{\mathrm{B}}_{\mathrm{A/B}})} \\ 0_{3\times1} \end{bmatrix}
$$

and

$$
g(x(t),t) = \begin{bmatrix} -\frac{1}{2}[\widetilde{\delta \boldsymbol{q}_{\mathrm{B/I},r}}] & 0 & 0 & 0 & 0 \\ -\frac{1}{2}[\widetilde{\delta \boldsymbol{q}_{\mathrm{B/I},d}}] & -\frac{1}{2}[\widetilde{\delta \boldsymbol{q}_{\mathrm{B/I},r}}] & 0 & 0 & 0 \\ 0 & 0 & I_3 & 0 & 0 \\ -\overline{b_v}^{\times} + \overline{(\hat{\omega}^{\mathrm{B}}_{\mathrm{B/I}} + \hat{b}_\omega - b_\omega)\times r^{\mathrm{B}}_{\mathrm{A/B}}}^{\times} + \overline{\hat{\omega}^{\mathrm{B}}_{\mathrm{B/I}} + \hat{b}_\omega - b_\omega}^{\times} \overline{r^{\mathrm{B}}_{\mathrm{A/B}}}^{\times} & 0 & 0 & cI_3 & 0 \\ 0 & 0 & 0 & 0 & I_3 \end{bmatrix}.
$$

In these equations, g^{I} is the gravitational acceleration expressed in the inertial frame and $c \in \mathbb{R}$ is a scaling factor specific to every accelerometer. Furthermore, the matrices

$$
F(t) \triangleq \left.\frac{\partial f(x,t)}{\partial x}\right|_{\hat{x}(t)} \in \mathbb{R}^{15\times15} \quad \text{and} \quad G(t) \triangleq g(\hat{x}(t),t) \in \mathbb{R}^{15\times15}
$$

can be determined to be

$$
F(t) = \begin{bmatrix} -\overline{\hat{\omega}^{\mathrm{B}}_{\mathrm{B/I}}}^{\times} & 0 & -\frac{1}{2}I_3 & 0 & 0 \\ -\overline{\hat{v}^{\mathrm{B}}_{\mathrm{B/I}}}^{\times} & -\overline{\hat{\omega}^{\mathrm{B}}_{\mathrm{B/I}}}^{\times} & 0 & -\frac{1}{2}I_3 & 0 \\ 0 & 0 & 0 & 0 & 0 \\ 2\overline{\hat{q}^*_{\mathrm{B/I}} g^{\mathrm{I}} \hat{q}_{\mathrm{B/I}}}^{\times} & 0 & -\overline{\hat{b}_v}^{\times} + \overline{\hat{\omega}^{\mathrm{B}}_{\mathrm{B/I}} \times r^{\mathrm{B}}_{\mathrm{A/B}}}^{\times} + \overline{\hat{\omega}^{\mathrm{B}}_{\mathrm{B/I}}}^{\times} \overline{r^{\mathrm{B}}_{\mathrm{A/B}}}^{\times} & -\overline{\hat{\omega}^{\mathrm{B}}_{\mathrm{B/I}}}^{\times} & cI_3 \\ 0 & 0 & 0 & 0 & 0 \end{bmatrix}
$$

and

$$
G(t) = \begin{bmatrix} -\frac{1}{2}I & 0 & 0 & 0 & 0 \\ 0 & -\frac{1}{2}I_3 & 0 & 0 & 0 \\ 0 & 0 & I_3 & 0 & 0 \\ -\overline{\hat{b}_v}^{\times} + \overline{\hat{\omega}^{\mathrm{B}}_{\mathrm{B/I}} \times r^{\mathrm{B}}_{\mathrm{A/B}}}^{\times} + \overline{\hat{\omega}^{\mathrm{B}}_{\mathrm{B/I}}}^{\times} \overline{r^{\mathrm{B}}_{\mathrm{A/B}}}^{\times} & 0 & 0 & cI_3 & 0 \\ 0 & 0 & 0 & 0 & I_3 \end{bmatrix}.
$$

Table 1: Sensor characteristics.

Signal	Sensor	Noise SD	Bias	Refresh Rate
$\bar{\omega}^{\mathrm{B}}_{\mathrm{B/I}}$	Humphrey RG02-3227-1 rate-gyro	0.027 deg/s	$<$ 2 deg/s	100 Hz
$\bar{n}^{\mathrm{B}}_{\mathrm{A/I}}$	Crossbow AHRS400CC-100 IMU	1.5 mg	$<$ 8.5 mg	100 Hz
$q_{\mathrm{B/I}}$	8 VICON BONITA B10 cameras	$< 7 \times 10^{-5}$	-	Variable ($\leq$ 250 Hz)
$\bar{r}^{\mathrm{B}}_{\mathrm{B/I}}$	8 VICON BONITA B10 cameras	$<$ 1 mm	-	Variable ($\leq$ 250 Hz)

The general form of the non-linear output is $z_m(t_k) = h_m(x_n(t_k)) + v_m(t_k)$. The specific form used in this experiment is given by

$$\overline{(\hat{\boldsymbol{q}}^{-}_{\mathrm{B/I}}(t_k))^{*}\boldsymbol{q}_{\mathrm{B/I},m}(t_k)} = \overline{\delta\boldsymbol{q}_{\mathrm{B/I}}(t_k)} + v(t_k), \tag{22}$$

where $z(t_k) = \overline{(\hat{\boldsymbol{q}}^{-}_{\mathrm{B/I}}(t_k))^{*}\boldsymbol{q}_{\mathrm{B/I},m}(t_k)}$ and $h(x(t_k)) = \overline{\delta\boldsymbol{q}_{\mathrm{B/I}}(t_k)}$. From this equation, the measurement sensitivity matrix is given by

$$H(t_k) \triangleq \left.\frac{\partial h(x)}{\partial x}\right|_{\hat{x}^{-}} = \begin{bmatrix} I_6 & 0_{6\times 6} & 0_{6\times 3} \end{bmatrix} \in \mathbb{R}^{6\times 15}. \tag{23}$$

Moreover, with the optimal Kalman state update calculated by

$$\Delta^{\star}\hat{x}(t_k) \triangleq \begin{bmatrix} \Delta^{\star}\overline{\delta\hat{\boldsymbol{q}}_{\mathrm{B/I}}}(t_k) \\ \Delta^{\star}\bar{\hat{\boldsymbol{b}}}_{\boldsymbol{\omega}}(t_k) \\ \Delta^{\star}\bar{\hat{b}}_{n}(t_k) \end{bmatrix} = K(t_k)(z(t_k) - \hat{z}(t_k)) = K(t_k)\overline{(\hat{\boldsymbol{q}}^{-}_{\mathrm{B/I}}(t_k))^{*}\boldsymbol{q}_{\mathrm{B/I},m}(t_k)}, \tag{24}$$

the estimate of the state at time t_k after a measurement is calculated from

$$\hat{\boldsymbol{q}}^{+}_{\mathrm{B/I}}(t_k) = \hat{\boldsymbol{q}}^{-}_{\mathrm{B/I}}(t_k)\Delta^{\star}\delta\hat{\boldsymbol{q}}_{\mathrm{B/I}}(t_k), \tag{25}$$

$$\bar{\hat{\boldsymbol{b}}}^{+}_{\boldsymbol{\omega}}(t_k) = \bar{\hat{\boldsymbol{b}}}^{-}_{\boldsymbol{\omega}}(t_k) + \Delta^{\star}\bar{\hat{\boldsymbol{b}}}_{\boldsymbol{\omega}}(t_k), \tag{26}$$

$$\bar{\hat{b}}^{+}_{n}(t_k) = \bar{\hat{b}}^{-}_{n}(t_k) + \Delta^{\star}\bar{\hat{b}}_{n}(t_k), \tag{27}$$

and $K(t_k) \in \mathbb{R}^{15\times 6}$.

EXPERIMENTAL TESTBED

The ASTROS facility, shown in Figure 1, is located in the DCSL at the Georgia Institute of Technology. It comes with 12 cold air thrusters, a rate gyro, and an inertial measurement unit. A surrounding VICON system provides real time pose information. The general characteristics of the sensors are provided in Table 1. The ASTROS facility is thoroughly described in Refs. [10, 18, 19].

HIGH FIDELITY SIMULATION

Among the primary benefits of the experiments performed is the validation of the high-fidelity simulation that has been developed for the 5-DOF platform. The Simulink model for this simulation is shown in Figure 2, and it is this same model/code that is used for the hardware-in-the-loop experiments. However, for the actual implementation of the experiments, the block corresponding to the platform dynamics is replaced by Simulink xPC target blocks. The simulation introduces high fidelity, or real-world effects through the addition of filters in order to more accurately simulate the response of mechanical actuators, and through the addition of realistic noise, bias, and drift to the measurements from the different sensors.

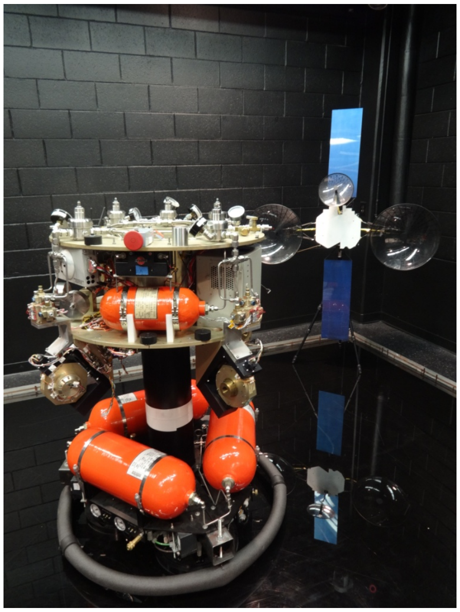 

Figure 1: The ASTROS platform (left) and the control room (right) at the DCSL.

EXPERIMENTAL VALIDATION

Several closed-loop tests were performed on the ASTROS platform using the thrusters and the VICON system. These tests were used to validate the inertia-free pose-tracking controller[12] and the DQ-MEKF.[10]

For the experiment reported in this paper*, the thrusters were used to track a time-varying attitude and position reference. The DQ-MEKF was used to estimate the pose and velocities of the upper stage with respect to the inertial frame. The DQ-MEKF was fed pose measurements at 10 Hz from the VICON system, angular velocity measurements at 100 Hz from the rate-gyros, and linear acceleration measurements at 100 Hz from the IMU. The initial estimate of the state of the DQ-MEKF is given in Table 2. The same table also shows an a posteriori guess of the initial state based on the measurements.

The control gains are chosen to be $\bar{K}_r = 0.74 I_{3\times 3}$, $\bar{K}_q = 0.2 I_{3\times 3}$, $\bar{K}_v = 84.37 I_{3\times 3}$, $\bar{K}_\omega = 15 I_{3\times 3}$, and $K_i = 500 I_{7\times 7}$. At the beginning of the experiment, the initial state of the inertia-free pose-tracking controller is set to zero.

The reference pose is illustrated in Figure 3 and is split in five phases:

1. Phase #1: During the first 20 sec, the controller is off and the DQ-MEKF is allowed to converge.

2. Phase #2: During the next 20 sec, the controller is turned on. During this phase, the desired position of the center of rotation of the platform with respect to the inertial frame is given by

*A video of the experiment can be found online at: `http://www.ae.gatech.edu/labs/dcsl/movies/Second_5DOF_experiment_annotated.mp4`

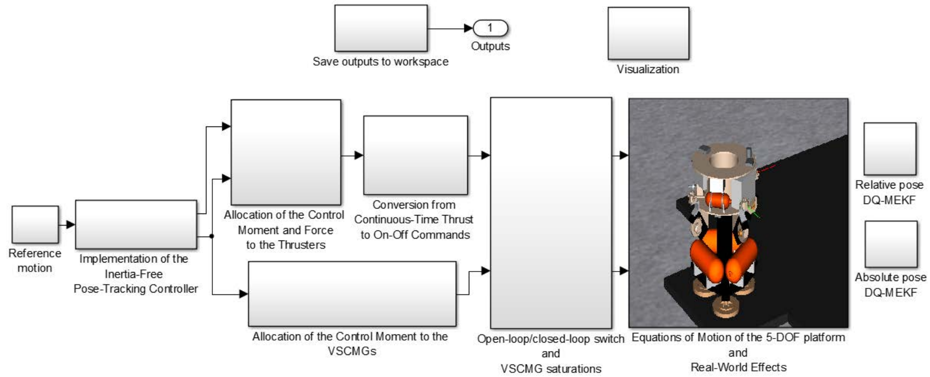

Figure 2: Simulink implementation of high fidelity simulation.

Table 2: Initial estimate and a posteriori guess of the state of the DQ-MEKF in the 5-DOF experiment.

Variable	Initial Estimate	A Posteriori Guess
$q_{\mathrm{S/I}}(0)$	$[0.7071, 0, 0, -0.7071]^{\mathsf{T}}$	$[0.7000, -0.0092, 0.0023, -0.7141]^{\mathsf{T}}$
$\bar{r}^{\mathrm{I}}_{CR/O_{\mathrm{I}}}(0)$	$[2.965, 2.008, 0]^{\mathsf{T}}$ (m)	$[2.965, 2.008, -1.004]^{\mathsf{T}}$ (m)
$\bar{b}_{\omega}(0)$	$[-1, 1, 1]^{\mathsf{T}}$ (deg/s)	$[-0.9046, 1.2503, 0.8183]^{\mathsf{T}}$ (deg/s)
$\bar{b}_{v}(0)$	$[0, 0, 0]^{\mathsf{T}}$ (m/s)	$[0, 0, 0]^{\mathsf{T}}$ (m/s)
$\bar{b}_{n}(0)$	$[0, 0, 0]^{\mathsf{T}}$ (-)	$[-0.0012, 0.0152, 0.0003]^{\mathsf{T}}$ (-)

$(x^{\mathrm{I}}_{O_{\mathrm{D}}/O_{\mathrm{I}}}, y^{\mathrm{I}}_{O_{\mathrm{D}}/O_{\mathrm{I}}}) = (2.965, 2.008)$ m and the desired orientation of the S-frame with respect to the I-frame is given by $\psi_{\mathrm{D/I}} = -90$ deg, $\theta_{\mathrm{D/I}} = 0$, and $\phi_{\mathrm{D/I}} = 0$.

3. Phase #3: During the next 60 sec, the center of rotation of the platform should describe a quarter of a circle with a radius of 1.2 m around the center of the floor with constant angular speed. The upper stage should remain leveled and $-\bar{J}_{\mathrm{S}}$ should point to the center of the circle. In other words, during this phase, $(x^{\mathrm{I}}_{O_{\mathrm{D}}/O_{\mathrm{I}}}, y^{\mathrm{I}}_{O_{\mathrm{D}}/O_{\mathrm{I}}}) = (1.765 + 1.2\cos(\frac{2\pi}{240}t), 2.008 + 1.2\sin(\frac{2\pi}{240}t))$ m, $\psi_{\mathrm{D/I}} = -\frac{\pi}{2} + \frac{2\pi}{240}t$ rad, $\theta_{\mathrm{D/I}} = 0$, $\phi_{\mathrm{D/I}} = 0$, and t is the elapsed time since the beginning of the phase.

4. Phase #4: During the next 60 sec, the center of rotation of the platform should describe a straight-line along the $-\bar{J}_{\mathrm{I}}$ direction with constant linear speed. The upper stage should remain leveled and $-\bar{J}_{\mathrm{S}}$ should point to the center of the circle. In other words, during this phase, $(x^{\mathrm{I}}_{O_{\mathrm{D}}/O_{\mathrm{I}}}, y^{\mathrm{I}}_{O_{\mathrm{D}}/O_{\mathrm{I}}}) = (1.765, 3.208 - \frac{1.2}{60}t)$ m, $\psi_{\mathrm{D/I}} = 0$, $\theta_{\mathrm{D/I}} = 0$, $\phi_{\mathrm{D/I}} = 0$, and t is the elapsed time since the beginning of the phase.

5. Phase #5: During the next 20 sec, the upper stage should maintain the desired position and attitude reached at the end of phase #4. In other words, during this phase, $(x^{\mathrm{I}}_{O_{\mathrm{D}}/O_{\mathrm{I}}}, y^{\mathrm{I}}_{O_{\mathrm{D}}/O_{\mathrm{I}}}) = (1.765, 2.008)$ m, $\psi_{\mathrm{D/I}} = 0$, $\theta_{\mathrm{D/I}} = 0$, and $\phi_{\mathrm{D/I}} = 0$.

The upper stage and the lower stage were levitated approximately 12.74 sec and 15.29 sec after the beginning of the experiment, respectively. Figure 4(a) compares the attitude and angular velocity estimated by the DQ-MEKF with the ground truth. The error between them is shown in Figure 4(b).

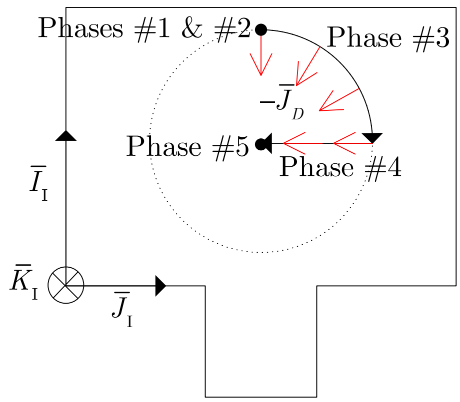

Figure 3: Reference pose. The desired trajectory of the center of rotation is illustrated in black, whereas the desired orientation of the upper stage is illustrated in red.

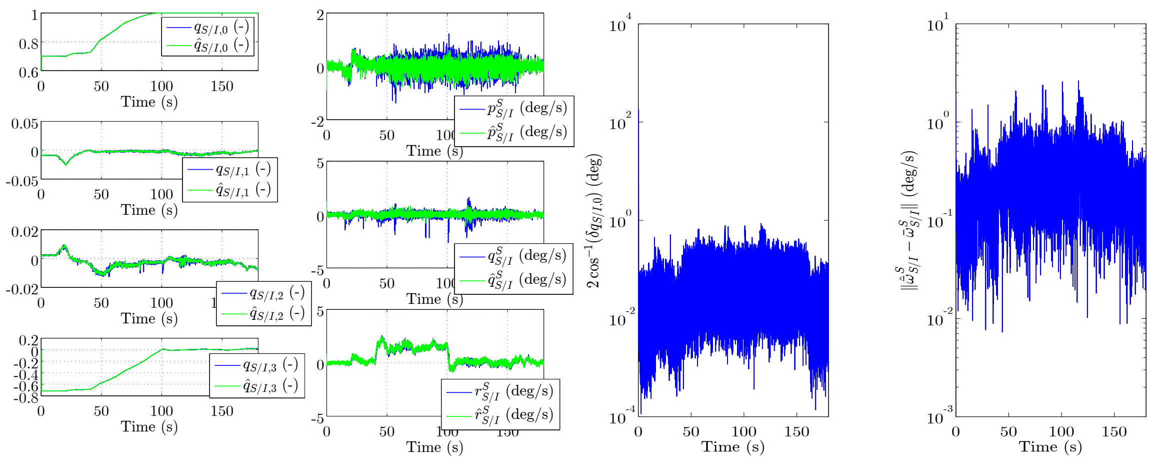

(a) Actual time history. (b) Error.

Figure 4: Experiment with thrusters: attitude and angular velocity comparison between estimate and ground truth.

After 20 sec, the RMS attitude estimation error is 0.13 deg and the RMS angular velocity estimation error is 0.37 deg/s. Likewise, Figure 5(a) compares the position and linear velocity estimated by the DQ-MEKF with the ground truth. The error between them is shown in Figure 5(b). After 20 sec, the RMS position estimation error is 1.0 mm and the RMS linear velocity estimation error is 5.6 mm/s. Note that the apparent vertical motion of the center of rotation is not only due to the slope of the epoxy floor, but also to errors in the experimental determination of the center of rotation.

Thrust allocation to the 12 different thrusters was performed through the solution of a linear program (LP)[10] for which the open-source GLPK package was used. Figure 6(a) shows the real-time solution to the LP problem throughout the experiment. It can be noted that the maximum thrust of thruster 7 is momentarily exceeded. Figure 6(b) shows the on-off commands produced from the solution of the LP problem using a scheme based on a Pulse-Width-Modulator (PWM) and a Schmitt trigger.[10] In Figure 6(b), the large thrusters (first and third columns plotted) are fired

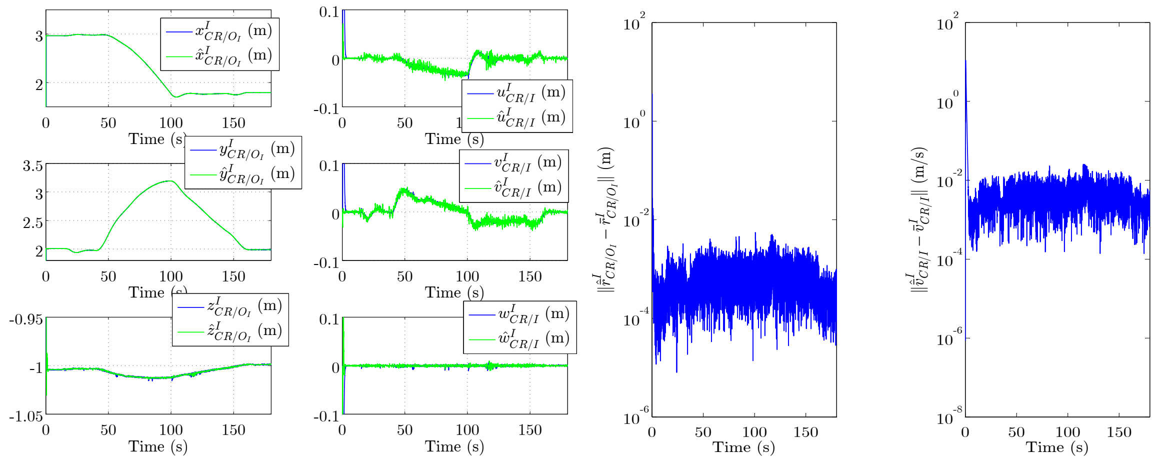

(a) Actual time history.

(b) Error.

Figure 5: Experiment with thrusters: position and linear velocity comparison between estimate and ground truth.

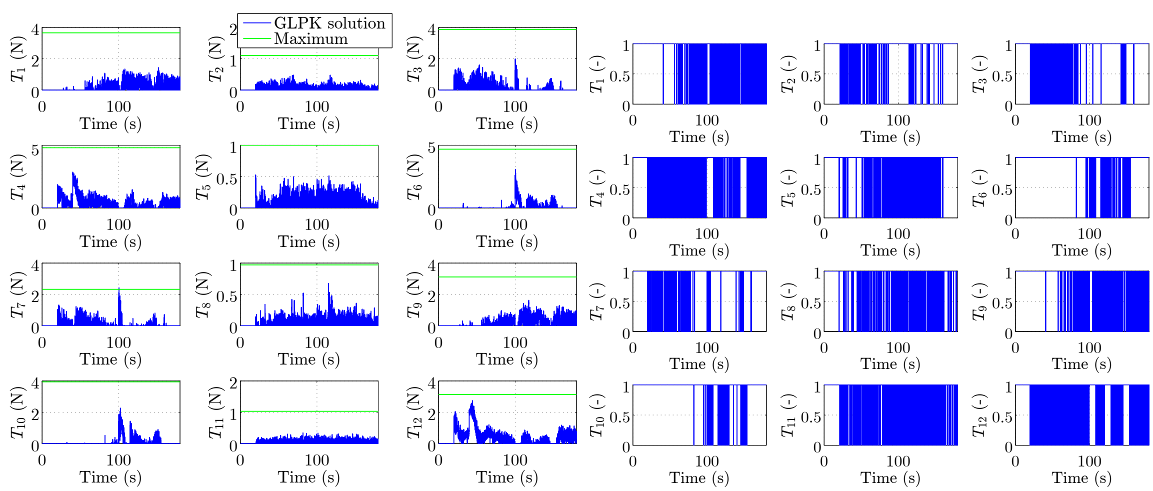

(a) LP problem solution.

(b) On-off. Open at 0 and closed at 1.

Figure 6: Experiment with thrusters: solution to LP problem calculated by the GLPK package and on-off commands issued to thrusters.

considerably more than the smaller thrusters. The main reason for this is that the large thrusters have to track not only the desired attitude, but also the desired position. Because the epoxy floor as the experimental arena is not perfectly flat, the large thrusters must also counteract gravity, which acts as a continuous disturbance force. As a result, the large thrusters must fire almost continuously in order to keep the position-tracking error within the values shown in Figure 8(b).

Figure 7(a) compares the desired attitude and angular velocity with the attitude and angular velocity estimated by the DQ-MEKF. The error between them is shown in Figure 7(b). The desired pitch and roll angles were tracked within approximately ± 1 deg after the transient response between

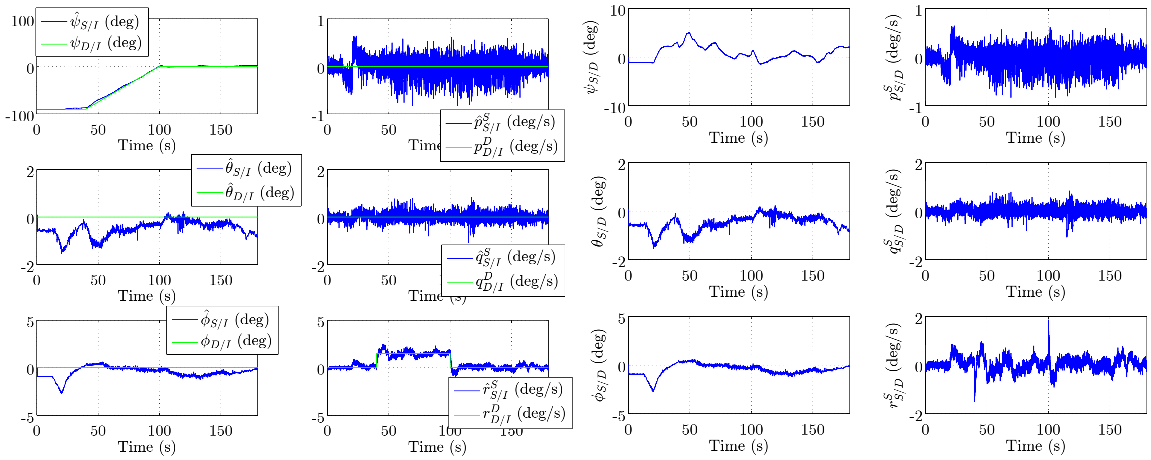

(a) Actual time history.

(b) Error.

Figure 7: Experiment with thrusters: desired versus estimated attitude and angular velocity.

phases #2 and #3. As for the yaw-tracking error, it did not exceed approximately ± 2 deg after the transient response between phases #2 and #3 and it reached a maximum of approximately 5 deg during this transient. Similarly, the coordinates of the desired angular velocity were tracked within approximately ± 1 deg/s.

Figure 8(a) compares the desired position and linear velocity with the position and linear velocity estimated by the DQ-MEKF. The error between them is shown in Figure 8(b).

Moreover, the desired position and the position estimated by the DQ-MEKF are projected onto the $\bar{I}_{\mathrm{I}}$-$\bar{J}_{\mathrm{I}}$ plane for both the experiment and the simulation in Figure 9. After the transient response between phases #2 and #3 and phases #3 and #4, $x^{\mathrm{I}}_{CR/O_{\mathrm{D}}}$ and $y^{\mathrm{I}}_{CR/O_{\mathrm{D}}}$ are kept within approximately ± 3 cm for the experiment, and within ± 4 cm for the simulation. Moreover, at the end of the experiment, $x^{\mathrm{I}}_{CR/O_{\mathrm{D}}}$ and $y^{\mathrm{I}}_{CR/O_{\mathrm{D}}}$ are 2.6 cm in the experiment (-0.5 cm in the simulation), and -2.0 cm in the experiment (-2.0 cm in the simulation), respectively. As for the desired linear velocity coordinates, they were tracked within ± 0.05 m/s in both cases. The current match between the simulation and the experiment is deemed acceptable. A posteriori simulations have shown that the largest contributor for the position-tracking error is the slope of the epoxy floor. Future improvements to the experiment will consist of modifying the controller so that *dual* disturbance forces are accounted for, allowing to reduce the steady state error.

CONCLUSION

This experiment has successfully demonstrated the use of a dual quaternion formulation to obtain acceptable absolute pose-tracking performance of a 5-DOF reference motion. For this experiment, the DQ-MEKF fused rate gyro, IMU, and VICON measurements with a *continuous-discrete* formulation. The external forces commanded by the adaptive dual quaternion controller are effectively converted into on-off thrust commands by the solution of a linear program. Furthermore, the high-fidelity simulation results are an accurate representation of the experimental results. This provides a valuable tool to efficiently test new algorithms and to evaluate the performance of the platform for different types of maneuvers, without the overhead cost incurred by an experiment. Finally, these

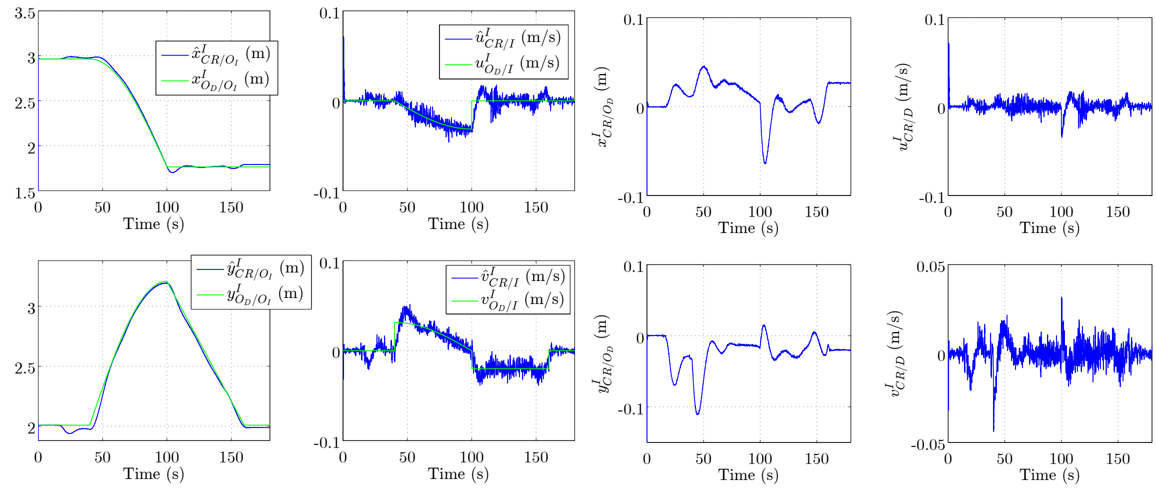

(a) Actual time history.

(b) Error.

Figure 8: Experiment with thrusters: desired versus estimated position and linear velocity.

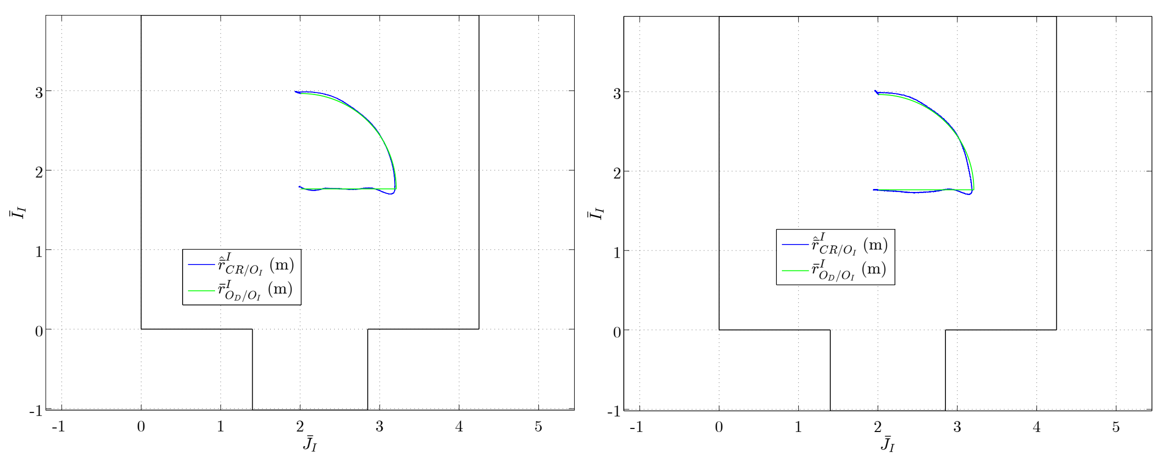

(a) Experiment.

(b) Simulation.

Figure 9: Experiment and Simulation: Desired versus estimated position within the limits of the epoxy floor.

results provide a benchmark against which future closed-loop experiments with a vision system on the ASTROS platform can be compared.

REFERENCES

[1] J. L. Schwartz, M. A. Peck, and C. D. Hall, "Historical Review of Air-bearing Spacecraft Simulators," *Journal of Guidance, Control, and Dynamics*, Vol. 26, July-August 2003, pp. 513–522.

[2] D. Jung and P. Tsiotras, "An Experimental Validation of Spacecraft Attitude and Power Tracking with Variable Speed Control Moment Gyroscopes," *AAS Spaceflight Mechanics Meeting*, Sedona, AZ, Jan, January 28 - February 1, 2007, pp. 07–130. AAS Paper 07-130.

[3] T. Ustrzycki, R. Lee, and H. Chesser, "Spherical Air Bearing Attitude Control Simulator for Nanosatellites," *AIAA Modeling and Simulation Technologies Conference*, Portland, OR, AIAA, August 8-11, 2011. AIAA Paper 2011-6272.

[4] S. Cho, J. Shen, N. McClamroch, and D. Bernstein, "Equations of Motion for the Triaxial Attitude Control Testbed," *Proceedings of the 40th IEEE Conference on Decision and Control, 2001.*, Vol. 4, Orlando, Florida, IEEE, December 4-7, 2001, pp. 3429–3434.

[5] M. Romano, D. A. Friedman, and T. J. Shay, "Laboratory Experimentation of Autonomous Spacecraft Approach and Docking to a Collaborative Target," *Journal of Spacecraft and Rockets*, Vol. 44, January-February 2007, pp. 164–173.

[6] D. Gallardo and R. Bevilacqua, "Six Degrees of Freedom Experimental Platform for Testing Autonomous Satellites Operations," *Proceedings of the 8th International ESA GNC Conference*, Carlsbad, Czech Republic, June 5-10, 2011.

[7] D. Gallardo, R. Bevilacqua, and R. E. Rasmussen, "Advances on a 6 Degrees of Freedom Testbed for Autonomous Satellites Operations," *Proceedings of AIAA Guidance, Dynamics and Control Conference*, Portland, Oregon, June 5-8, 2011. AIAA Paper 2011-6591.

[8] S. P. Viswanathan, A. Sanyal, and L. Holguin, "Dynamics and Control of a Six Degrees of Freedom Ground Simulator for Autonomous Rendezvous and Proximity Operation of Spacecraft," *Proceedings of AIAA Guidance, Navigation, and Control Conference*, Minneapolis, Minnesota, August 13-16, 2012. AIAA Paper 2012-4926.

[9] N. Filipe and P. Tsiotras, "Adaptive Model-Independent Tracking of Rigid Body Position and Attitude Motion with Mass and Inertia Matrix Identification using Dual Quaternions," *AIAA Guidance, Navigation, and Control Conference*, Boston, MA, AIAA, August 19-22, 2013. AIAA Paper 2013-5173.

[10] N. Filipe, *Nonlinear Pose Control and Estimation for Space Proximity Operations: An Approach Based on Dual Quaternions*. PhD thesis, Georgia Institute of Technology, 2014.

[11] N. A. Aspragathos and J. K. Dimitros, "A comparative study of three methods for robot kinematics," *Systems, Man, and Cybernetics, Part B: Cybernetics, IEEE Transactions on*, Vol. 28, April 1998, pp. 135–145.

[12] N. Filipe and P. Tsiotras, "Adaptive position and attitude-tracking control for satellite proximity operations using dual quaternions," *Journal of Guidance, Control, and Dynamics*, 2014, 10.2514/1.G000054.

[13] N. Filipe, M. Kontitsis, and P. Tsiotras, "Extended Kalman Filter for Spacecraft Pose Estimation Using Dual Quaternions," *Journal of Guidance, Control, and Dynamics*, 2015. Accepted.

[14] E. Bayro-Corrochano and Y. Zhang, "The Motor Extended Kalman Filter: A Geometric Approach for Rigid Motion Estimation," *Journal of Mathematical Imaging and Vision*, Vol. 13, No. 3, 2000, pp. 205–228, 10.1023/A:1011293515286.

[15] J. Goddard, *Pose and Motion Estimation From Vision Using Dual Quaternion-Based Extended Kalman Filtering. University of Tennessee, Knoxville*. PhD thesis, Ph. D. Thesis, 1997.

[16] Y. Zu, U. Lee, and R. Dai, "Distributed Motion Estimation of Space Objects Using Dual Quaternions," *SPACE Conferences & Exposition*, San Diego, CA: American Institute of Aeronautics and Astronautics, August 4 -7, 2014. 2014-4296, 10.2514/6.2014-4296.

[17] U. Lee and M. Mesbahi, "Dual Quaternion based Spacecraft Rendezvous with Rotational and Translational Field of View Constraints," *SPACE Conferences & Exposition*, San Diego, California: American Institute of Aeronautics and Astronautics, August 4-7, 2014, 10.2514/6.2014-4362.

[18] D.-M. Cho, D. Jung, and P. Tsiotras, "A 5-DOF Experimental Platform for Autonomous Spacecraft Rendezvous and Docking," *Proceedings of AIAA Infotech@ Aerospace Conference, Seattle, Washington*, Seattle, WA, AIAA, April 6-9, 2009, pp. 1–20, paper 2009–1869.

[19] P. Tsiotras, "ASTROS: A 5DOF Experimental Facility for Research in Space Proximity Operations," *AAS Guidance and Control Conference*, Breckenridge, CO, AIAA, January 31 - February 5, 2014. AAS Paper 14-114.